Measures of genetic diversification in somatic tissues at bulk and single cell resolution

Marius E. Moeller[1,†], Nathaniel V. Mon Père[2,3,†], Benjamin Werner[2,*], Weini Huang[1,4,*]

[1]Department of Mathematics, Queen Mary University of London, United Kingdom. [2]Evolutionary Dynamics Group, Centre for Cancer Genomics and Computational Biology, Barts Cancer Centre, Queen Mary University of London, Charterhouse Square, London, United Kingdom EC1M 6BQ. [3]Department of Physics, Vrije University of Brussels, Belgium. [4]Group of Theoretical Biology, The State Key Laboratory of Biocontrol, School of Life Science, Sun Yat-sen University, Guangzhou, 510060 China.

[†] These authors contributed equally. The order is ranked by reproduction fitness at publication, [*]Correspondence should be addressed to weini.huang@qmul.ac.uk and b.werner@qmul.ac.uk

Abstract

Intra-tissue genetic heterogeneity is universal to both healthy and cancerous tissues. It emerges from the stochastic accumulation of somatic mutations throughout development and homeostasis. By combining population genetics theory and genomic information, genetic heterogeneity can be exploited to infer tissue organisation and dynamics *in vivo*. Here we show that single cell and bulk sequencing data inform on different aspects of the underlying stochastic processes. Bulk derived variant allele frequency spectra (VAF) show transitions from growing to constant stem cell populations with age in samples of healthy oesophagus epithelium. Single-cell mutational burden distributions allow a sample size independent measure of mutation and proliferation rates. Mutation rates in adult haematopietic stem cells are higher compared to inferences during development, suggesting additional proliferation independent effects. Furthermore, single cell derived VAF spectra contain information on the number of tissue specific stem cells. In haematopiesis, we find approximately 2×10^5 HSCs, if all stem cells divide symmetrically. If HSCs also undergo asymmetric divisions, fewer HSCs could maintain homeostasis. A more precise estimate requires an independent measure of the asymmetric division rate p, which currently is complicated by the sparsity of single cell data.

Introduction

Intra-tissue genetic heterogeneity emerges from a multitude of dynamical processes [1, 2]. Cells randomly accumulate mutations while they self-renew, differentiate or die, while clones of varying fitness may compete and expand [3–6]. These core evolutionary principals form the basis for describing the aging of somatic tissues, tumour initiation and tumour progression [7–12]. Naturally, there is great

interest in understanding precisely how these dynamical processes act. This typically involves hypothesizing models of cell behavior, and deriving quantitative estimates of their underlying physical parameters [3, 5, 13–17]. These could by quantities such as mutation rates per cell division, active stem cell numbers, symmetric and asymmetric division rates, etc. Some such parameters are already well characterised in certain tissues. We know for example that during early development healthy somatic cells accumulate on average between 1.2 and 1.3 mutations per genome per division [5, 18]. Other parameters, such as the number of stem cells in a tissue type, are well known in some tissues but much harder to quantify in others. Accurate knowledge of such quantities can lead to novel insights, for example recent work pointed out that seemingly small differences in the number of stem cells in crypts of small and large intestine have major consequences on selection intensities of mutations, and can potentially explain differences in life time risks of cancer progression [19]. In contrast, in the haematopoietic system estimates vary by two orders of magnitude [18, 20]. In general, a lack of time resolved information complicates evolutionary inferences, and we must often rely on indirect information, for example the patterns of tissue-specific genetic heterogeneity within and across individuals [21]. These observed patterns of genetic heterogeneity are the combined result of the underlying stochastic processes and the measurement technique [22]. Both enforce specific limitations on the inferability of the underlying dynamics. Different types of genomic data – such as bulk and single cell whole genome sequencing – may contain different information on the system, and each comes with their own limitations. When bulk sequencing data is used for inference, some evolutionary parameters such as the population size and proliferation rates of stem cells are entangled and cannot be obtained in isolation [3, 16]. If on the other hand single cell data is employed, some additional information becomes available, for example the individual cell mutational burdens and the co-occurrence of mutations. However, often the sampling size is sparse compared to the presumed number of long-term proliferating cells in many tissues [18, 23, 24], which in turn introduces other constraints. Here we show that combining such data obtained from different resolutions (bulk or single cell) can help to overcome limitations and further narrow possible ranges of inferred parameters. We develop concrete mathematical and computational models for extracting evolutionary parameters from bulk and single cell information and apply these methods to whole genome bulk sequencing data in healthy oesophagus [10] and whole genome single cell sequencing data in healthy haematopoiesis [18].

Results

A stochastic model of mutation accumulation in healthy somatic tissue

We model the stem cell dynamics of healthy tissue as a collection of individual cells that divide, differentiate, and die stochastically at predefined rates (see Fig.1). Novel mutations can occur with every cell division, each daughter acquiring a random number drawn from a Poisson distribution with rate μ. We explicitly include symmetric and asymmetric stem cell divisions at potentially different rates, the former resulting in two stem or two differentiated cells, and the latter in one stem and one differentiated cell. Since differentiated cells are lost from the stem cell pool they are functionally equivalent to cell death. While only symmetric divisions allow variants to change in frequency, both division types introduce novel variants into the population and thus both contribute to the evolving heterogeneity.

Mutation accumulation occurs through all developmental stages from conception to death [25]. We therefore consider three phases of demographic changes of the stem cell population. In the first early developmental phase the stem cell population rapidly expands from a single cell exclusively by sym-

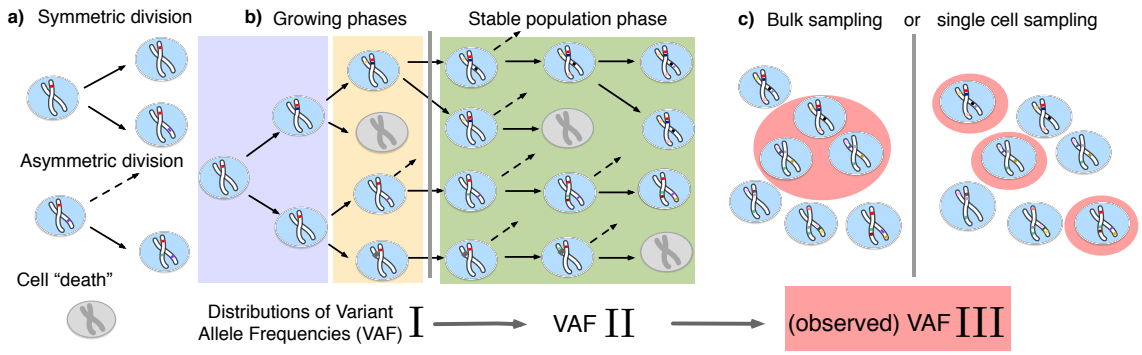

Figure 1. The distribution of variant allele frequencies changes with the growth phases and by sampling. (a) In the current population, cells divide symmetrically into two daughter cells or asymmetrically with only one daughter cell kept in the focused population. All other events are mathematically equivalent to and are treated as a part of cell death. **(b)** The rates of symmetric and asymmetric division change during the population growth and lead to a dynamical distribution of variant allele frequencies. **(c)** The observed VAF distribution is shifted again during sampling compared to the VAF of the whole population – a fact should be considered when inferring population properties through genetic data.

metric divisions at rate γ. This is followed by a growth and maintenance phase wherein the population continues to expand but also undergoes turnover through asymmetric divisions at rate ϕ, as well as cell removal (due to differentiation or death) and replacement at rate ρ. In the final mature phase, cell turnover continues but the size of the total stem population N remains constant.

We employ two independent implementations of our theoretical model. One is a direct stochastic simulation utilizing a Gillespie algorithm. This approach creates a simulated dataset containing all single cell or bulk sequencing properties, however it can be computationally expensive. In addition, we compute the time-dynamical expected value of the distribution of variant allele frequencies (the VAF spectrum) directly, which we find obeys the partial differential equation

$$\partial_t V(\kappa,t) = -\partial_\kappa \mathcal{A}(\kappa,t)V(\kappa,t) + \partial_\kappa^2 \mathcal{B}(\kappa,t)V(\kappa,t) + \mathcal{C}(t)\delta(\kappa-1)\ , \tag{1}$$

where $\kappa = fN(t)$ denotes the number of cells sharing a variant (the variant frequency f times the total population size N), $\delta(x)$ is the Dirac impulse function, and

$$\mathcal{A}(\kappa,t) = \gamma\kappa\ , \qquad \mathcal{B}(\kappa,t) = \kappa(1-\kappa/N(t))\rho + \gamma\kappa/2\ , \qquad \mathcal{C}(t) = 2\mu N(t)(\rho+\gamma+\phi/2)\ ,$$

This set of equations allows for computationally efficient numerical solutions (SI 1.3).

Transition of developmental growth and constant population size signatures in bulk whole genome sequencing data of healthy adult oesophagus

We first discuss established properties of the VAF spectrum relating to somatic tissues. In certain model systems it is given by a power law $\propto f^{-\alpha}$ with a critical exponent α. The value of the exponent depends on the demographic dynamics of the population. For a well-mixed exponentially growing population without cell death the VAF spectrum $v(f)$ is given by $2\mu/(f+f^2)$ (a f^{-2} power law) and is

independent of time [6]. In contrast, for a population of constant size the spectrum obeys $v(f) \propto 2\mu/f$ [26] (a f^{-1} power law; see also SI 1.5.1), though this solution is only approached at sufficiently long times. In the following, we focus on the dynamics of genetic diversification in healthy tissues and show that the expected VAF spectrum contains both contributions of growing and constant population dynamics.

Healthy adult somatic tissues are thought to initially expand rapidly during ontogenic growth, continue to expand during infancy and childhood, and reach homeostasis by adulthood. It is thus natural to ask what the expected VAF spectrum would look like in tissues experiencing homeostasis after a period of growth. We first investigated the underlying VAF dynamics in a minimal theoretical model where the population switches from pure exponential growth to constant size once a maximal cell number is reached. Stochastic simulations and numerical solutions of Eq. (1) show that the VAF distribution exhibits a gradual transition from the f^{-2} to the f^{-1} power law (Fig. 2a). These transitional states themselves do not adhere to some intermediate power-law (e.g. $f^{-\alpha}$ for $1 < \alpha < 2$), but instead present a wavelike front whereby the equilibrium establishes earliest at the lowest frequencies and moves to higher frequency over time. As the distribution approaches f^{-1}, convergence towards equilibrium continues to slow down, resulting in a higher density of solutions for evenly-spaced observation times. The transition from an exponential signature f^{-2} to a constant signature f^{-1} is initially fast for low frequency variants and slows down considerably at older ages for high frequency states. More complex forms of such demographic changes, for example the inclusion of a mixed growth-and-maintenance phase or a logistically growing population, result in qualitatively similar behavior (see Supplementary Fig. 5).

To test whether adult human tissues show such transitional signatures, we grouped the VAFs of healthy adult oesophagus samples from Martincorena and colleagues [10] into three age groups (young, middle and old, Fig. 2b). In accordance with our theoretical expectations, the averaged VAF spectrum of the young donor group is closest to the expected f^{-2} distribution of ontogenic growth, with low frequency variants only starting to approach the f^{-1} homeostatic scaling. The averaged spectra of the middle and old age groups on the other hand notably shift towards the expected f^{-1} homeostatic line. Interestingly, while there is a clear separation between the spectra of the youngest and middle age groups, those of the middle and older groups are much closer. This agrees with our prediction that the speed of convergence of the spectra towards homeostatic scaling slows down with age.

VAF based mutation rate inferences in healthy tissues

The theoretical prediction for the VAF spectrum of an exponentially growing population, which is recovered in many cancers given sufficient sequencing depth [22], contains information on the effective mutation rate μ [27]. Similarly, the VAF spectrum of a constant population includes the same mutation rate μ (SI). Thus we can in principle infer μ from the previously described oesophagus data, for example by applying a regression approach. However, since the scaling of the VAF spectrum of healthy tissues can be shown to be age dependent (Fig. 2a-b), we use two reference shapes for a growing and a constant population, respectively. The fitting is performed by a linear regression least-squares approach. The general solution is computed from the VAF spectrum of the data, $V_d(\mu)$, and the reference shape V_r, which assumes $\mu = 1$, as follows:

$$\mu = \frac{\mathrm{Cov}(V_d(\mu), V_r)}{\mathrm{Var}(V_r)} \tag{2}$$

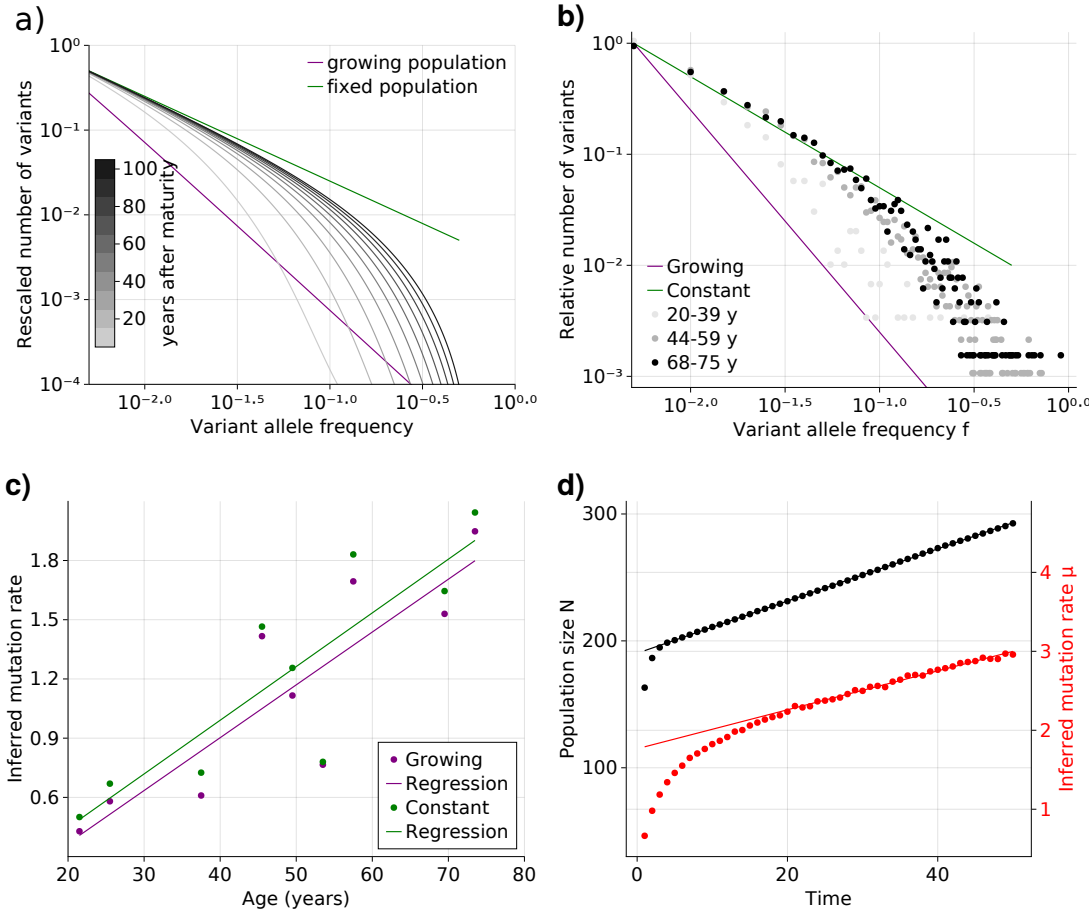

Figure 2. Bulk sequencing based VAF and mutation rate inferences in healthy esophagus. (a) Simulated VAF with an initial logarithmic growth phase and subsequent constant population phase at different time points. As the population gets closer to the maximum simulated carrying capacity of $N = 10^4$, the VAF moves from a $1/f^2$ growing population shape to a $1/f$ constant population shape. Note, the shift considerably slows at older age. **(b)** VAF from healthy tissue in the esophagus of 9 individuals sorted into age brackets. The youngest bracket, 20-39, is closer to the developmental $1/f^2$ scaling. The older age brackets are both close to the constant population $1/f$ scaling, resembling the theoretical expectations. **(c)** Inferred mutation rates increase linearly with age. **(d)** Simulations of slowly growing stem cell populations reveal that mutation rates appear to increase with age, although the true underlying per division mutation rate remaining constant.

If $V_d(\mu)$ has the shape of V_r, then $\mathrm{E}(V_d(\mu)) = \mu\,\mathrm{E}(V_r)$, which can be used to prove equation 2:

$$\mathrm{Cov}(V_d(\mu), V_r) = \mathrm{E}(V_d(\mu), V_r) - \mathrm{E}(V_d(\mu))\,\mathrm{E}(V_r) = \mu(\mathrm{E}(V_r^2) - \mathrm{E}(V_r)^2) = \mu \cdot \mathrm{Var}(V_r) \tag{3}$$

The VAF shapes for the growing and constant population give close estimates, as can be seen in fig. 2, which compares the age of all individuals with corresponding inferred effective mutation rates. The estimates are in the range of 1 to 2 mutations per genome per cell division and agree with previous observations based on early developmental stem cell divisions [18]. Estimates based on a growing population are slightly higher compared to estimates based on a constant population, but differences are small.

Surprisingly, we observe a clear trend of a linearly increasing effective mutation rate with age. This trend cannot be explained by the transition of variants from a growing into a constant population alone. An actual increase of the true mutation rate per cell division with age would be a direct explanation. However, this seems unlikely: It is well established that the mutational burden across individuals and tissues increases linearly with age [9, 11, 28], and an increasing mutation rate would in contrast result in an accelerated increase of mutational burden with age, which is not observed experimentally.

An alternative explanation is a continued slow linear increase of the stem cell population with age (Fig. 2d). In such a scenario, the effective mutation rate would appear to increase linearly with age as well, although the true mutation rate per cell division remains unchanged. At first glance, a linearly increasing stem cell population appears unnatural. However, such a linear increase would emerge from a small bias of stem cells towards self-renewal (growth) and concomitantly a slowdown of the stem cell proliferation rate proportional to the change of population size [29]. The latter is a natural feedback mechanism ensuring a constant output of differentiated somatic cells. Direct *in vivo* imaging in multiple human tissues including Oesaphagus seem to support an increased density and slower proliferation of stem cells with age [30]. This explanation is attractive for another reason: A feedback of decreased cell proliferation with increasing population size would also function as a tumour suppressor mechanism, and may be another reason cancer driver mutations in healthy tissues are abundant but rarely progress to cancer [10, 31]. Progression would require additional genomic or environmental changes to overcome this regulatory feedback.

Single-cell mutational burden allows sample size independent inferences of stem cell proliferation and mutation rates

With the increasing availability of single-cell data, it becomes possible to investigate distributions of certain quantities for which bulk sequencing only provides average measurements. One such is the number of mutations present in individual cells. Recent work by Lee-Six and colleagues [18] showed that in a 59 year old donor haematopoietic stem cells had accumulated on average around 1000 mutations per cell; however there was significant variation between individual genomes, some carrying 900 mutations, while others up to 1200. This variation is the result of the stochastic nature of mutation accumulation and cell division, and can be exploited to estimate per division mutation and stem cell proliferation rates. To this end we look at the distribution of the number of mutations per cell, which we will from here on refer to as the *mutational burden distribution*. Formally, we describe the mutational burden m_j in a cell j by a stochastic sum over its past divisions $m_j = \sum_i^{y_j} u_{ij}$, in which both the total number of divisions y_j in the cell's past and the number of mutations per division u_{ij} are random variables. Even without knowing the actual distributions of y and u, general expressions for the expec-

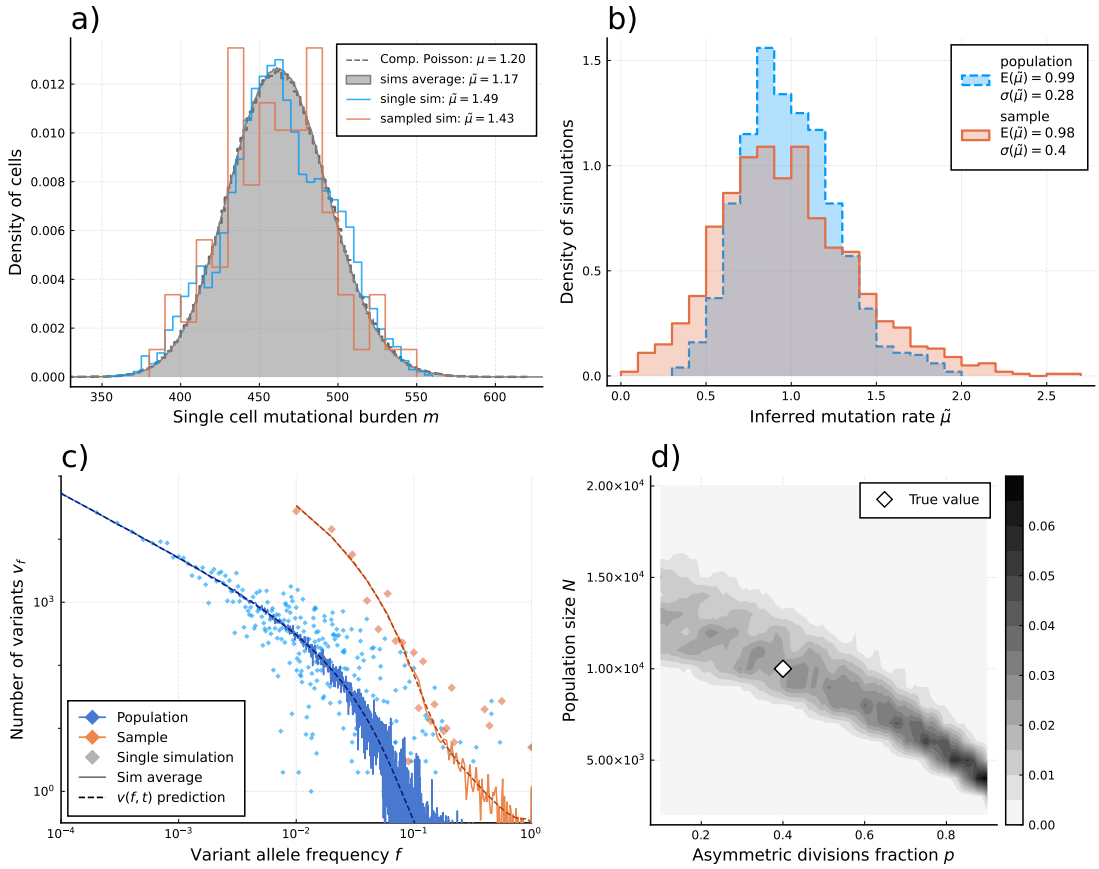

Figure 3. Inference of evolutionary parameters on simulated stem cell populations. Simulated populations were run up to age 59, growing exponentially from a single cell to constant size $N_M = 10'000$ at age $t_M = 5$, with mutation rate $\mu = 1.2$ and division rates $\lambda = 5$ and $p = 0.4$. Where sampling is mentioned, the sample size 89 was taken. **a)** The single-cell mutational burden distribution. The compound Poisson distribution (dashed line) matches the burden distribution when averaging over multiple independently evolved populations (filled curve). **b)** Distribution of estimated mutation rates from 10'000 individual simulations, obtained from burden distributions of the complete populations (blue) as well as sampled sets of cells (orange). **c)** VAF spectra measured in the complete population (blue) and a sampled set of cells (orange). A single simulation result is shown (diamonds) alongside the theoretically predicted expected value (Eq. (1)) (dashed line) and the average across 100 simulations (solid line). **d)** Distribution of N_M and p inference results for 100 simulated and sampled populations, through estimation of $\tilde{\mu}$ and $\tilde{\lambda}$ from the single cell burden distribution and fitting the number of lowest frequency ($1/S$) mutations to the theoretical prediction (Eq. (1)).

tation and variance of m_j that only depend on the expectation and variance of y and u exist and are given by $\mathrm{E}(m) = \mathrm{E}(y)\,\mathrm{E}(u)$ and $\mathrm{Var}(m) = \mathrm{E}(y)\,\mathrm{Var}(u) + \mathrm{E}(u)^2\,\mathrm{Var}(y)$ (SI 1.7). These expressions allow direct estimates of the effective division and mutation rate. Assuming the mutation rate per daughter cell is Poisson distributed with expectation μ, the average number of divisions per lineage — expressed in terms of an effective division rate λ — becomes

$$\int \lambda(t)dt = \mathrm{E}(y) = \mathrm{E}(m)/\mu \tag{4}$$

In addition, if the mutation rate μ is unknown, it can similarly be obtained from

$$\mu = \left(\frac{\mathrm{Var}(m)}{\mathrm{E}(m)} - 1\right)\frac{\mathrm{E}(y)}{\mathrm{Var}(y)}. \tag{5}$$

We first show that these estimators recover per division mutation and proliferation rates in stochastic simulations (Fig. 3a and b). More importantly, they only require information on comparably few single cells. Approximately, 100 cells are sufficient to reliably reconstruct the mutational burden distribution, which for example would constitute a small sample of the haematopoietic stem cell pool. In fact, the inference does not significantly improve if we increase data resolution beyond a few hundred single cells (Fig. 3a and b). This is in stark contrast to inferences based on single cell phylogeny: Although they contain more information in principle, important aspects of a single cell phylogeny, e.g. the number of observable branchings, are strongly affected by sampling and stem cell population size.

We apply our estimators to single-cell mutational data in blood obtained from the study by Lee-Six et al. [18], in which 89 haematopoietic stem cells (HSCs) were extracted from a bone marrow aspirate of a 59-year-old individual (Fig. 4a). Using Eq. (4) to estimate the expected number of divisions per lineage from the sample burden (SI 1.8.1), we find a total division rate (including both symmetric and asymmetric divisions) in the constant population phase of $\lambda = 10.6$ (7.6-15.3) divisions per HSC per year, which is within ranges previously suggested [3, 20]. Notably, the single-cell mutational burden alone can not disentangle symmetric and asymmetric division rates. Applying Eq. (5) to the sample burden distribution and taking $\mathrm{Var}(y)/\,\mathrm{E}(y) = 1$ (akin to assuming exponentially distributed division times, a common but simplified null model) we obtain an estimated mutation rate of $\tilde{\mu} = 4.3$ per cell per division (Fig. 4a). This is significantly higher compared to the 1.2 mutations per division suggested previously [5, 18]. We posit different possible explanations for this discrepancy. Stem cell divisions and mutation accumulation are stochastic processes, therefore variation between individuals is expected. However, simulations of our model for a wide range of parameter values suggest the distribution of these inferred mutation rates is unlikely to present a wide enough variance to explain this difference (Fig. 7). Recently, Mitchell and colleagues [12] suggested that many mutations in somatic tissue are acquired independently of cell divisions. In fact, the previous estimates of 1.2 to 1.3 mutations per genome per division were derived from early developmental cell divisions where effects of aging would be negligible. The increased mutation rate inferred here could in part be explained by proliferation independent effects. However, it is important to note that the true distribution of divisions per lineage may also be over-dispersed compared to the Poisson model (i.e. $\mathrm{Var}(y) > \mathrm{E}(y)$), which would lead to an overestimation of μ in Eq. (5). Furthermore, the observed burden distribution is incompatible with a simple division-independent mutation model, which would lead to a Poisson distribution of the burdens that has a variance much smaller than what we observed (Fig. 4a). A combination of division independent mutations together with non-Poissonian cell divisions could possibly reproduce the result.

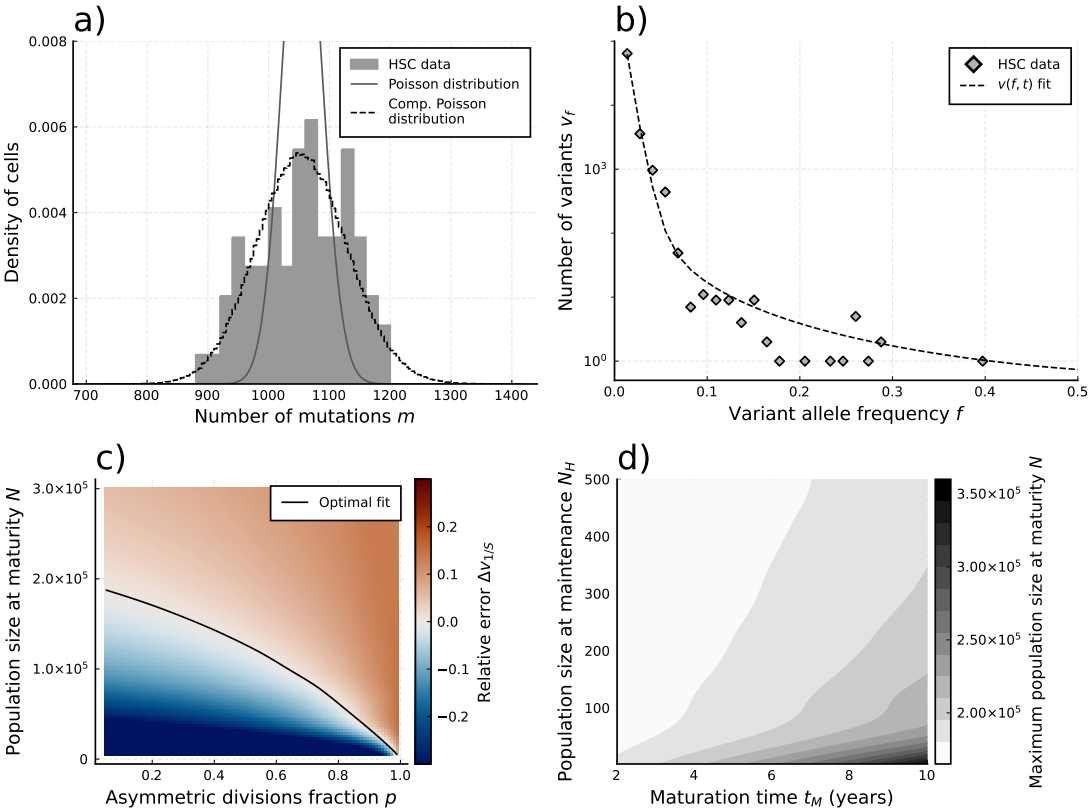

Figure 4. Evolutionary inferences in single cell HSC data (a) The single-cell mutational burden distribution of the data (bars) and the Compound Poisson distribution obtained from its mean and variance, used to obtain the estimated per division mutation rate $\tilde{\mu}$. **(b)** distribution of mutation frequencies of the data and theoretically predicted average fitted to only the lowest frequency ($1/S$) data point. **(c)** Difference Δv_f between measured value of the VAF spectrum at lowest frequency ($1/S$) and its prediction from Eq. (1), for varying total population size N and asymmetric division proportion p, with fixed maturation time $t_M = 5$ and operational hematopoietic population size $N_H = 50$. The solid line denotes the plane of best fit where this difference is 0. **(d)** Maximally inferred population size N (taking $p = 0$ in (c)) for variation of the maturation time t_N and the operational hematopoietic population size N_H.

Sparse sampling, single cell derived VAF spectra and evolutionary inferences

Current methods limit us to whole genome information of at most a few thousand single cells per tissue or tumour [24]. In many situations this will only constitute a small fraction of the underlying long term proliferating cell population. For example, although the exact number of HSCs remains unknown, most recent estimates suggest a population size of 10^5 cells [3, 18]. In tumours, this number can be as large as 10^{10} cells [32]. As we have shown in the previous paragraph, the single-cell mutational burden distribution allows certain inferences even if sampling is sparse. If we however construct the VAF spectrum from such a small sample, the distribution of variants will be significantly transformed with respect to that of the total population (Fig. 3c). Since Eq. (1) gives the expected curve measured from the total population, one must include a correction, which is given by the expectation of hypergeometric sampling (i.e. without replacement). This can be obtained through the transformation (see Supplement 1.6)

$$\tilde{V}(i) = \sum_{j=i}^{N} V(j) \cdot \binom{j}{i}\binom{N-j}{S-i} \Big/ \binom{N}{S} \tag{6}$$

with $\tilde{V}$ the VAFs observed in the sample and S the sample size. Furthermore, from stochastic simulations we note that the variance on the distribution increases with variant frequency f, making the lowest frequency state (i.e. $1/S$) the best candidate for comparative fitting and evolutionary inferences (see Supplement Fig. 9).

Taking the mutation rate from Werner et al. [5] and the total division rate obtained from the burden distribution as constant, we explored solutions of Eq. (1) (sampled by Eq. (6)) for a wide range of realistic values in the remaining parameter space $\{N, p, t_M, N_H\}$. Comparing the lowest sampled frequency state ($f = 1/89$) with the data (Fig. 4b) we identify a curve in the space of the numbers of HSCs N and p (fraction of divisions that are asymmetric) where theoretically predicted VAF distributions are identical (Fig. 4c). Interestingly, this curve in N-p space naturally identifies a maximal stem cell population size capable of producing the data, which occurs when stem cells divide exclusively symmetrically ($p = 0$). Variations of t_M (the time until maturity of the HSC population) and N_H (the HSC pool size at which maintenance begins to occur) had only a small effect on the this inference (Fig. 4d). This is partly because mutations arising during these phases are more likely to be found at higher frequencies upon measurement [13, 33]. We find the data to be congruent with an adult HSC pool of at most 200'000-300'000 cells, depending on the exact timings of the maturation phase (Fig. 4d). This estimate agrees with the original study and other independent inferences based on population data [3, 18]. However, this upper bound corresponds to the case of exclusively symmetric stem cell divisions. Accounting for the possibility of mutating asymmetric divisions reduces the estimated stem cell pool. For example, the data would be consistent with 50'000 stem cells if 90% ($p = 0.9$) of all stem cell divisions are asymmetric. In principle, even smaller stem cell pool sizes are possible, though decreasing an order of magnitude would imply an extremely large portion ($> 99\%$) of asymmetric HSC divisions. We note that in the data non-developmental branchings are observed, which immediately implies that not all HSC divisions can be asymmetric ($p < 1$) and thus a scenario of an extremely small population of only a handful of HSCs maintaining heamatopoisis can be rejected. With an orthogonal population based method, Watson and colleagues estimated 25'000 as a reasonable lower bound for the number of HSCs. Based on our inference, this would imply 0.95 as an upper bound for the proportion of all stem cell divisions that are asymmetric.

Discussion

Here, we have shown that single cell and bulk whole genome sequencing can inform on different aspects of somatic evolution. Single cell information does support previous bulk based estimates of possible ranges of HSC numbers. Surprisingly, the same single cell data leads to a mutation rate inference during homeostasis approximately 4 times higher compared to previous developmental estimates.

An important recent study has suggested an amended model of mutation accumulation in somatic tissues, wherein the majority of mutations are acquired continuously over time throughout a cell's lifespan rather than during DNA replication [12]. We note that for a time dependent rate of mutation accumulation that is constant across all cells at a given point in time, this model predicts Poisson distributed single-cell mutational burdens. In contrast, we find the single-cell mutational burden distribution in human HSCs to be highly over-dispersed compared to a Poisson model. A time-associated model of mutation accumulation with a constant rate alone cannot generate such a pattern. At least one additional source of stochasticity would be needed. This could be fluctuations in the time dependent mutation rates, non-constant cell proliferation rates, e.g. bursts of stem cell divisions potentially in reaction to injury or disease, or a combination of both effects. Either way, our observations suggest that our current theoretical models of somatic evolution in healthy tissues are incomplete. There is evidence for unknown processes contributing to intra-tissue genetic heterogeneity. The precise nature of these processes remains an open question.

Acknowledgments

The authors are grateful to Marc Williams and Christo Morison for discussions at different stages of the manuscript.

N.V.MP. acknowledges support by the Barts Charity. B.W. is supported by a Barts Charity Lectureship (grant no. MGU045) and a UKRI Future Leaders Fellowship (grant no. MR/V02342X/1). This project has been facilitated by an Alan Turing Institute Data Science for Science Program grant.

1 Supplementary Information

1.1 Model system

We model a dynamical population of $N(t)$ cells, each able to carry multiple mutations. It evolves by the occurrence of divisions — which replace cells in the pool with their (potentially mutated) daughter cells — and removals — which can correspond to differentiation or any form of cell inactivation. As outlined in Figure 1, we model different types of divisions affecting the system:

(i) A symmetric (non-differentiating) division replaces a cell in the population with two daughter cells, each of which maintains the mutational profile of its parent and acquires a Poisson distributed number of new mutations.

(ii) A symmetric differentiation removes a cell from the population, as both of its daughter cells have differentiated.

(iii) an asymmetric division replaces a cell with a single daughter cell — as the other daughter has differentiated — and also acquires a Poisson distributed number of mutations.

The rates at which these divisions occur depends on what stage of development the population is in. A simplest approach is to consider two broad phases of evolution: an initial growth phase where $N(t)$ increases according to some growth function, and a mature phase at a time t_M where $N(t)$ is constant and stem cell divisions occur only to maintain homeostasis of the population. While the earliest stage of population expansion can reasonably be approximated as purely developmental — i.e. where little to no turnover occurs in the population — maintenance of the functional population (e.g. in the blood system) will at some point be required even as the stem cell pool continues grow. Thus we also include a mixed phase occurring before maturity but only after the stem cell pool has reached a size N_H, where stem cells can differentiate and homeostasis must be maintained. Note that this size is expected to be relatively small, as the earliest haematopoietic cells appear 16 days post conception [34], and peripheral blood is already driven mostly by functional HSC's by 14 weeks post conception [25]. Constancy of the population size in the mature phase is ensured by applying a Moran model of divisions [35], where each non-differentiating symmetric division — which results in two daughter cells with the HSC phenotype — is simultaneously accompanied by a removal, either through a symmetric differentiation or some form of cell inactivation. Thus in our model we distinguish 3 types of events which occur independently with exponentially distributed waiting times:

1. Growth divisions, which are non-differentiating symmetric divisions (i) occurring at rate γ, and cause the population to increase in size by 1 cell;
2. Moran events, which consist of the simultaneous occurrence of a non-differentiating symmetric division (i) (which causes the population to increase in size by 1) and a cell removal (ii) (which causes the population to decrease in size by 1) either through symmetric differentiation or inactivation. These events occur at rate ρ;
3. Asymmetric divisions (iii), in which one of the daughter cells is differentiated and the other is not, occurring at rate ϕ.

In the early developmental phase there are only growth divisions; during the mixed phase, growth divisions occur alongside Moran events and asymmetric divisions; and in the mature phase, only

Symbol	Description	Units
N_M	Carrying capacity of the mature population	
t_M	Age when the cell population reaches mature size	years
N_H	Population size at homeostatic divisions (start of the mixed-growth phase)	
γ	Symmetric division rates in early developmental phase	/year
ρ	Symmetric division rate in homeostatic state	/year
ϕ	Asymmetric division rate in homeostatic state	/year
μ	Mutation rate	/division/daughter

Table 1. Evolutionary parameters appearing in the model system.

the Moran and asymmetric division events occur. Note that under these dynamics the rates of the different types of divisions changes across phases: the rate of non-differentiating symmetric divisions (sometimes referred to as self-renewals) is given by γ during early development, $\gamma + \rho$ during mixed growth, and finally ρ at maturity; while the rate of asymmetric divisions respectively jumps from 0 to ϕ in the mixed phase, and remains at ϕ in the mature phase. This can be summarized as:

$$\begin{aligned} \gamma(t) &= \gamma\,\Theta(t < t_M) \\ \rho(t) &= \rho\,\Theta(N(t) > N_H) \\ \phi(t) &= \phi\,\Theta(N(t) > N_H) \end{aligned} \tag{7}$$

We assume exponential growth (see section 1.4 for discussion of other possible growth curves) from the stem cell population's most recent common ancestor (the zygote, or any later occurring stem cell), and make the simplifying assumption that all division rates remain constant in their respective range of operation. The population size then depends on the division rates as $N(t) = \exp\left(\gamma(t)t\right)$ with $\Theta(x)$ the Heaviside step function.

We introduce μ as the rate parameter of the Poisson distribution from which the number of mutations arising in a daughter cell is drawn, i.e. the mutation rate per daughter per division. Each new mutation is presumed to be distinct from all previously existing mutations in the system, an assumption known as the *infinite sites model*.

A summary of all parameters governing this model is given in table 1.

1.2 Stochastic simulation of the dynamical model

In direct simulations of the system we model individually distinct cells, each carrying a particular set of mutations. These are evolved according to the model described in Section 1.1 by means of a Gillespie algorithm [36]: Events are performed successively with exponentially distributed waiting times, and the acting cell in each event is selected uniform randomly from the population. Daughter cells arising from a division inherit all mutations from their parent cell, and acquire new mutations which are distinct from any existing mutations.

Simulations are initiated with a single cell carrying no mutations. In the early and mixed growth phases, taking the rate of growth divisions γ as fixed ensures exponential growth of the complete population. To investigate the effect of differing growth curves (see section 1.4), we also implemented a logistic growth phase, where cell division gradually decreases and cell death gradually increases

until the population reaches its mature size. The average population growth then follows

$$N(t) = \frac{N_M}{1 + e^{-\gamma t}}. \tag{8}$$

The code for the simulations was written in the Julia computing language, and can be found at https://github.com/natevmp/hsc-vaf-dynamics.

1.3 The expected VAF distribution of the complete population

To obtain the dynamics of the VAF distribution, we first look at the probabilistic time evolution of a single variant's size (i.e. the number of cells sharing that mutation) $P_k(t)$, which is given by a Fokker-Plank equation. We first sketch the procedure for obtaining the result for a Moran model, where the population size is constant. Next, we show how to obtain the expression for a deterministically growing population. Finally we use these results to obtain the distribution of variants for a population that changes in size.

1.3.1 Probability density distribution of a single variant in a Moran process

The discrete probability distribution of variant's size is governed by the transition probabilities $\mathbb{P}\{l|k\}$, which denotes the likelihood of the number of cells carrying this mutation changing from k to l. In a Moran model, a constant population size N is maintained by the simultaneous occurrence of one cell division and one cell death/removal. Thus, the possible transitions following the occurrence of such an event are given by the probabilities

$$\begin{cases} \mathbb{P}\{k+1\,|\,k\} = \dfrac{k}{N}\left(1 - \dfrac{k}{N}\right) = T_{k+1,k} = T_k, \\ \mathbb{P}\{k-1\,|\,k\} = \dfrac{k}{N}\left(1 - \dfrac{k}{N}\right) = T_{k-1,k} = T_k, \text{ and} \\ \qquad \mathbb{P}\{k\,|\,k\} = 1 - (T_{k+1,k} + T_{k-1,k}). \end{cases} \tag{9}$$

Assuming events occur with exponentially distributed waiting times at rate ρ, P_k can be described through the master equation

$$\frac{1}{\rho}\frac{\mathrm{d}P_k}{\mathrm{d}t} = T_{k-1}P_{k-1} + -2T_kP_k + T_{k+1}P_{k+1} \tag{10}$$

When the population size N is large, this leads to a system of N differential equations, which is computational taxing to solve. Instead, a diffusion approximation can be made (on the assumption that N is large, i.e. that there are many states $k = 0, 1, \ldots, N$), to describe $p(\kappa)$, the probability density of variant's size on the continuous support $\kappa \in [0, N]$. To this end a Fokker-Planck equation is constructed of the form

$$\partial_t p(\kappa, t) = -\partial_\kappa A(\kappa, t)p(\kappa, t) + \partial_\kappa^2 B(\kappa, t)p(\kappa, t)/2 \tag{11}$$

where the coefficients are given through the infinitesimal propagator $t(\kappa + \Delta\kappa, t + \Delta t \,|\, \kappa, t)$:

$$\begin{aligned} A(\kappa, t) &= \lim_{\Delta t \to 0} \frac{1}{\Delta t} \int d(\Delta\kappa) \Delta\kappa \, t(\kappa + \Delta\kappa, t + \Delta t \,|\, \kappa, t) \\ B(\kappa, t) &= \lim_{\Delta t \to 0} \frac{1}{\Delta t} \int d(\Delta\kappa) (\Delta\kappa)^2 \, t(\kappa + \Delta\kappa, t + \Delta t \,|\, \kappa, t) \end{aligned} \tag{12}$$

The integrals are the first and second moments of a displacement $\Delta\kappa$, and can be obtained using the heuristic [37]:

$$\begin{aligned} \langle \Delta\kappa \rangle_{k,\Delta t} &\approx \langle \Delta\kappa \rangle_{k,1/\rho} \, \Delta t + \vartheta\left(\Delta t^2\right) = \sum_{\Delta k} \Delta k \, T_{k+\Delta k,k} \, \rho \, \Delta t + \vartheta\left(\Delta t^2\right) \\ \left\langle (\Delta\kappa^2) \right\rangle_{k,\Delta t} &\approx \left\langle (\Delta\kappa^2) \right\rangle_{k,1/\rho} \Delta t + \vartheta\left(\Delta t^2\right) = \sum_{\Delta k} (\Delta k)^2 \, T_{k+\Delta k,k} \, \rho \, \Delta t + \vartheta\left(\Delta t^2\right) \end{aligned} \tag{13}$$

Typically a transformation to frequency space is first performed, $f = \rho/N$, where f is the frequency of cells carrying this mutation in the population. Thus, we obtain

$$A(f, t) = 0, \quad B(f, t) = \frac{2\nu}{N^2} f(1 - f) \tag{14}$$

and finally the well-known result

$$\partial_t p(f, t) = (\rho/N^2) \, \partial_f^2 f(1 - f) p(f, t) \tag{15}$$

1.3.2 Probability density distribution of a single variant in a deterministic growing population

We now consider a growing population due to additional divisions occurring—at rate γ per cell—alongside the previously described Moran events. For simplicity we assume the population size $N(t)$ increases deterministically according to the growth rate. The transition probabilities for the variant size are then given by

$$\begin{cases} \mathbb{P}\{k+1, t+\Delta t \,|\, k, t\} = \dfrac{k}{N(t)} \left(1 - \dfrac{k}{N(t)}\right) \rho N(t) \Delta t + \dfrac{k}{N(t)} \gamma N(t) \Delta t, \\ \mathbb{P}\{k-1, t+\Delta t \,|\, k, t\} = \dfrac{k}{N(t)} \left(1 - \dfrac{k}{N(t)}\right) \rho N(t) \Delta t, \text{ and} \\ \mathbb{P}\{k, t+\Delta t \,|\, k, t\} = 1 - \mathbb{P}\{k+1, t+\Delta t \,|\, k, t\} - \mathbb{P}\{k-1, t+\Delta t \,|\, k, t\}. \end{cases} \tag{16}$$

Using the previously described heuristic (13) the coefficients of the Fokker-Planck equation become

$$\begin{aligned} A(\kappa, t) &= \kappa\gamma \\ B(\kappa, t) &= 2\kappa[1 - \kappa/N]\rho + \kappa\gamma \end{aligned} \tag{17}$$

And the full equation

$$\partial_t p(\kappa, t) = -\partial_\kappa \gamma\kappa \, p(\kappa, t) + \partial_\kappa^2 [\kappa(1 - \kappa/N(t))\rho + \kappa\gamma/2] \, p(\kappa, t). \tag{18}$$

1.3.3 The expected VAF distribution in a varying population

For independently evolving variants, we denote the number of variants at size k (i.e. shared by k cells) as $V_k(t)$. We now note that in the limit of infinite variants, the fluxes between adjacent k-states are identical to the above-derived transition probabilities. Thus the above-derived equations can similarly describe the expected dynamics of a an ensemble of variant sizes $V(\kappa, t)$, where we once again introduce the parameter $\kappa \in [0, N(t)]$ to represent the continuous space analog of the variant size k. In our system of interest we however also wish to include an injected flux of newly arising mutations, which is limited to the state $\kappa = 1$ and has amplitude

$$\mathcal{C} = 2\mu(\rho + \gamma + \phi/2) \tag{19}$$

Note that because asymmetric divisions result in just a single daughter remaining in the system, they contribute only half as many novel mutations to the system as symmetric divisions. In the continuous domain we introduce this flux as a Dirac delta function $\mathcal{C}\delta(\kappa - 1)$. Note also that, while these diffusion equations are more commonly applied in the frequency domain $f \in [0, 1]$, for the purpose of numerical simulation it will be convenient to remain in the space of absolute sizes $\kappa = fN(t)$. Then finally, the time evolution of the VAF distribution is given by

$$\begin{aligned} \partial_t V(\kappa, t) = &-\partial_\kappa \gamma \kappa V(\kappa, t) + \partial_\kappa^2 [\kappa(1 - \kappa/N(t))\rho + \gamma\kappa/2] V(\kappa, t) \\ &+ 2\mu N(t)(\rho + \gamma + \phi/2)\delta(\kappa - 1) \ , \end{aligned} \tag{20}$$

which is the result stated in the main text.

1.3.4 Numerical approximation of the VAF distribution dynamics

While a solution to the fixed population Moran system (15) is known [38], it is unwieldy, and does not readily generalize to the more complex expressions (18) and (20). We therefore resorted to numerical approximations of their solution. We applied a method of lines approach with a finite difference discretization in the size coordinate κ. The incoming flux of variants at $\kappa = 1$ introduces a discontinuity in the derivative, which leads to stiffness in the system. This is the reason we eschewed the transformation to $f = \kappa/N(t)$, since when working in frequency space the point of incoming flux would change position as the population grows. To maximize performance near the discontinuity, we implemented a variable step size smallest near $\kappa = 1$, with the distances in space given by

$$\Delta\kappa_i = 1 + (i - 1) \cdot \alpha_i \tag{21}$$

where $i \in 1, \ldots, n - 1$, with n the number of discretized points, and

$$\alpha_i = 2\frac{N - (n - 1)}{(n - 1)(n - 2)} \tag{22}$$

In this formalism the delta function in (1) was approximated as a step function with height $2/(\Delta\kappa_1 + \Delta\kappa_2)$.

1.4 Changing the growth function during the maturation phase

In the main text we have shown that, for a constant population, the past occurrence of a growth phase influences the shape of the observed VAF spectrum. Here we investigate to what extent the precise

Symbol	Description
N	Total number of cells
k	Abundance or number of cells $< N$
$V_k(t)$	Number of mutations with abundance k
P_k	Likelihood for a mutation with abundance k to increase or decrease
$C_k(t)$	The average number of mutations with abundance k that increase or decrease
$\frac{dV_k(t)}{dt}$	Average change of $V_k(t)$ per time step
μ	Mutation rate per daughter cell

Table 2. Evolutionary parameters appearing in the analytical derivations of the expected VAF distribution in the Moran and pure-birth models.

form of this growth function alters the observation. To this end we compare the expected VAF spectrum, calculated from Eq. (1), for two different growth models: One where the population grows exponentially until the maximal capacity N_M is reached, at which point it immediately stops expanding; and one where the population grows according to the logistic function, which is a common model for population growth in ecological systems. Since in the latter case the function only asymptotically approaches capacity, we take maturity to be the point where the population reaches $0.99N_M$. The resulting growth functions and expected VAF spectra are shown in Fig. 5 for two time points measured after maturity. We observe that there is indeed a quantitative difference between the spectra of the two models. However, we note the same qualitative characteristics as described in the Results section of the main text: a pronounced move towards the fixed size shape in the lower frequencies, and a delayed response at higher frequency. The difference between the two models furthermore diminishes as the measurement occurs farther away from the end of the growth phase.

1.5 Analytical solutions for the expected VAF distribution in select cases

While in section 1.3 it was shown how the expected VAF distribution of our stochastic model can be calculated numerically, under certain (stricter) conditions some solutions can also be obtained analytically. We present here derivations for analytical solutions of the distribution in a constant population adhering to a Moran process, and a strictly growing population subject to the pure-birth process. Although the results derived in this section are themselves not novel (see e.g. [26], [27], and [6]), we present them here for completeness, with new derivations that facilitate a unified analysis and do not require readings of the previous literature. For convenience, a list of the parameters used in this section is given in Table 2.

1.5.1 The equilibrium VAF distribution in a Moran process

In a birth-death Moran process, one cell dies and one is born every time step. Then, let every birth coincide with an average of μ new unique neutral mutations. Every cell can hold any number of mutations, and since these are neutral, the cells that are dying/born are chosen completely at random. If two cells are chosen for death and birth, any particular mutation has a chance P_k to be in one of the cells but not in the other:

$$P_k = \frac{k}{N} \cdot (1 - \frac{k}{N}) \tag{23}$$

This was previously also shown in Eq. (9). If we want to know how the number of mutations changes, we need to know how many mutations increase or decrease in abundance on average. This simply means that we multiply P_k by the number of mutations with the given abundance k:

$$C_k(t) = \frac{k}{N} \cdot (1 - \frac{k}{N}) \cdot V_k(t) \tag{24}$$

Note that because of the symmetry of the process, $C_k(t)$ is both the average increase and decrease. Lastly, if we look at a certain abundance k, there are two ways to lose mutations and two ways to gain mutations: M_k increases if mutations of abundance $k+1$ lose one cell or if mutations of abundance $k+1$ gain one cell. M_k decreases if mutations of abundance k lose or gain an cell. Note that all of these things can happen at the same time. If we want to know the average change $\frac{dV_k(t)}{dt}$, we therefore need to incorporate all of these four possibilities. After we add the rate division rate ρ, we finally get the following equation for the average change per unit of time:

$$\frac{dV_k(t)}{dt} = \rho \cdot (C_{k-1}, t) + C_{k+1}(t) - 2C_k(t)) \tag{25}$$

This is a variation of Eq. (10) applied to all mutations, as opposed to just a single one. For $k = 1$ the first term C_0 is simply replaced by a fixed mutation rate μ, for $k = N$, the middle term has to be removed (and the last term $C_N(t)$ is always 0). Once we apply this to an entire distribution of mutations, it gives us an estimate of how, on average, this distribution changes every time step. Notably, it should approach some equilibrium state if we exclude the last state, which is absorbing. Let us consider the distribution from $k = 1$ to $k = N - 1$. The only way for this distribution to lose mutations is by either a mutation of abundance 1 to die out, or a mutation of abundance $N - 1$ to fixate. This implies an equilibrium at:

$$\sum_{k=1}^{N-1} \frac{dV_k(t)}{dt} = \rho \cdot (\mu - C_{N-1}(t) - C_1(t)) = 0 \tag{26}$$
$$\implies \mu = C_1(t) + C_{N-1}(t) \implies C_1(t) = \mu - C_{N-1}(t)$$

We can now apply this iteratively to the other $C_k(t)$ (for convenience, we ignore the ρ, since it has no bearing on the equilibrium, merely on how fast we approach it):

$$\frac{dV_1(t)}{dt} = \mu + C_2(t) - 2C_1(t) = 0 \implies C_2(t) = 2(\mu - C_{N-1}(t)) - \mu = \mu - 2C_{N-1}(t) \tag{27}$$
$$0 = C_1(t) + C_3(t) - 2C_2(t) \implies C_3(t) = 2(\mu - 2C_{N-1}(t)) - \mu + C_{N-1}(t) = \mu - 3C_{N-1}(t) \tag{28}$$
$$\dots \tag{29}$$
$$C_k(t) = \mu - kC_{N-1}(t) \tag{30}$$

Which can then be applied to $C_{N-1}(t)$ itself:

$$C_{N-1}(t) = \mu - (N-1)C_{N-1}(t) \implies C_{N-1}(t) = \frac{\mu}{N} \tag{31}$$

This can now be used to solve for $C_1(t)$, $C_1(t)$ ... $C_{N-2}(t)$ iteratively, resulting in an equilibrium solution C_k^*:

$$C_k^* = \mu \cdot \frac{N-k}{N} \tag{32}$$

Finally, this can be transformed back into the $V_k(t)$ to get the equilibrium solution $V^*(k)$:

$$V^*(k) = C_k^* \cdot \frac{N}{k} \cdot \frac{1}{1 - \frac{k}{N}} = \mu \cdot \frac{N-k}{N} \cdot \frac{N}{k} \cdot \frac{N}{N-k} = \mu \frac{N}{k} \tag{33}$$

1.5.2 The VAF distribution of a growing population under a pure-birth process

In a pure-birth process only births, and no deaths, occur in the population. Suppose then a strictly growing population starting from a single cell increasing by 1 every time step, with a mutation rate of μ. We denote the number of mutations with abundance k at time t as $V_k(t)$. Then we can set up a system for the average change per time step:

$$\begin{aligned} V_k(t+1) &= (1 - \frac{k}{t+1})V_k(t) + \frac{k-1}{t+1}V_{k-1}(t) \\ V_1(t+1) &= (1 - \frac{1}{t+1})V_1(t) + 2\mu \end{aligned} \tag{34}$$

For simplicity we view the process in event time, so that every time step is exactly one division event. However, the process can be projected so that the amount of time δt that passes between every event is drawn at random from a given distribution. Since this projection is always possible in both directions now matter the chosen distribution, this proof is valid for any process, as long as births are not allowed to be simultaneous. The $V_k(t)$ themselves are all strictly increasing every time step and hence approach infinity, but we can make a statement about the average shape of the distribution and the value at each specific point in time:

$$V_k(t) = (\frac{2}{k} - \frac{2}{k+1}) \cdot (t+1)\mu = \frac{2}{k \cdot (k+1)} \cdot (t+1)\mu \tag{35}$$

To prove that $2/(k \cdot (k+1))$ is indeed the expected distribution for this system, we will first show that the first several time steps follow this shape. Then we prove that every time a new cell and thus a new possible abundance $k = t$ is added to the system, the new distribution at the new abundance will follow the expected distribution as well. Finally, we will show that if an abundance and the neighbouring abundance follow the distribution already, it will continue to follow the distribution.

Let's show now that the first few time steps follow the claimed distribution:

$$
\begin{aligned}
& V_1(1) = 2\mu \\
& V_1(2) = (1 - \frac{1}{2}) \cdot 2\mu + 2\mu = 3\mu \\
& V_2(2) = (\frac{1}{2}) \cdot 2\mu = 1\mu \\
\implies & \frac{V_2(2)}{V_1(2)} = \frac{1}{3} = \frac{2}{2} - \frac{2}{3} \\
& V_1(3) = (1 - \frac{1}{3}) \cdot 3\mu + 2\mu = 4\mu \\
& V_2(3) = (1 - \frac{2}{3}) \cdot 3 + \frac{1}{3} \cdot 1\mu = \frac{4}{3}\mu \\
& V_3(3) = (\frac{2}{3}) \cdot 1 = \frac{2}{3}\mu \\
\implies & \frac{V_2(3)}{V_1(3)} = \frac{1}{3} = \frac{2}{2} - \frac{2}{3} \\
\implies & \frac{V_3(3)}{V_1(3)} = \frac{1}{6} = \frac{2}{3} - \frac{2}{4}
\end{aligned} \tag{36}
$$

Now, since the first steps seem to follow the distribution as expected, we can move on to showing that generally at time step t, the newly generated abundance $k = t$ will always fit the distribution:

$$
\begin{aligned}
V_t(t) &= 0 + \frac{t-1}{t} \cdot \frac{2}{(t-1) \cdot t} \cdot t \cdot \mu \\
&= \frac{2}{t} \cdot \mu = \frac{2}{t \cdot (t+1)} \cdot (t+1) \cdot \mu \\
&= \frac{2}{k \cdot (k+1)} \cdot (t+1) \cdot \mu
\end{aligned} \tag{37}
$$

The only part remaining is proving that if the preceding time steps fit the distribution, the following time step also follows the distribution:

$$
\begin{aligned}
\frac{V_k(t+1)}{V_1(t)} &= (1 - \frac{k}{t+1})\frac{V_k(t)}{V_1(t)} + \frac{k-1}{t+1}\frac{V_{k-1}(t)}{V_1(t)} = (1 - \frac{k}{t+1})(\frac{2}{k \cdot (k+1)}) + \frac{k-1}{t+1}(\frac{2}{(k-1) \cdot (k)}) \\
&= (1 - \frac{k}{t+1})(\frac{2}{k \cdot (k+1)}) + \frac{k+1}{t+1}(\frac{2}{(k+1) \cdot (k)}) = (1 - \frac{k}{t+1} + \frac{k+1}{t+1})(\frac{2}{k \cdot (k+1)}) \\
&= (1 + \frac{1}{t+1})(\frac{2}{k \cdot (k+1)}) \\
V_1(t+1) &= (1 - \frac{1}{t+1}) \cdot (t+1)\mu + 2\mu = (t+1-1+2)\mu = (t+2)\mu \\
\implies \frac{V_1(t+1)}{V_1(t)} &= \frac{t+2}{t+1} = 1 + \frac{1}{t+1} \\
\implies \frac{V_k(t+1)}{V_1(t+1)} &= \frac{2}{k \cdot (k+1)} \implies V_k(t+1) = \frac{2}{k \cdot (k+1)} \cdot (t+2)\mu
\end{aligned} \tag{38}
$$

Note that unlike for the constant population case, the expected distribution does not need time to asymptotically approach the steady-state solution, as it is already at equilibrium from $t = 1$.

1.6 Sampling affects the observed VAF distribution

Eq. (1) describes the evolution of mutation frequencies with respect to the whole population, however, these are typically not known from sequencing data. Instead, an observation provides the frequencies of mutations as measured in the sequenced sample of the population. This distinction should be recognized when interpreting experimental data, as the statistical distribution for the sample's VAF distribution differs from that of the true population (Fig. 3c). To obtain the expected distribution $\tilde{v}(f)$ from a sample of S cells, we must consider how each mutation's frequency in the true population can be altered in the sample, so that the resulting curve is given by the sum over all original mutation frequencies j/N weighted by their probability of being sampled to a different frequency i/S. If sampling is performed randomly this probability is given by the hypergeometric distribution (sampling without replacement), leading to the expression

$$\tilde{v}(i/S) = \sum_{j=i}^{N} v(j/N) \cdot \binom{j}{i}\binom{N-j}{S-i} \Big/ \binom{N}{S} \tag{39}$$

Besides the anticipated loss of resolution, the effect of this operation is to shift the expected mutation frequencies upward with respect to their true frequency in the population (see Fig. 3c in the main text), which can lead to improper inferences if not correctly accounted for.

1.7 The mutational burden distribution

1.7.1 The expected mutational burden distribution

The expected distribution of mutational burdens can be obtained from the argument that the burden m_j of an individual cell at the time of observation must equal the sum over all mutations that occurred during each of its past cell divisions:

$$m_j = \sum_{i}^{y_j} u_{ji} \tag{40}$$

Without knowledge of the distributions of y and u other than the requirement that the u_{ji} are identically distributed and independently drawn, it is straightforward to show that the expectation and variance of m_j are given by $\mathrm{E}(m) = \mathrm{E}(y)\,\mathrm{E}(u)$ and $\mathrm{Var}(m) = \mathrm{E}(y)\,\mathrm{Var}(u) + \mathrm{E}(u)^2\,\mathrm{Var}(y)$ (Supplement). With the number of novel mutations per division as Poisson distributed, the average number of divisions per lineage — expressed in terms of an effective division rate λ — can thus be estimated from a sample as

$$\int \lambda(t)dt = \mathrm{E}(y) = \mathrm{E}(m)/\mu \tag{41}$$

If the mutation rate μ is not known, it can similarly be obtained from

$$\mu = \left(\frac{\mathrm{Var}(m)}{\mathrm{E}(m)} - 1\right)\frac{\mathrm{E}(y)}{\mathrm{Var}(y)} \tag{42}$$

Note that while a common modeling practice is to take the number of divisions as Poisson distributed — i.e. assuming exponentially distributed times between divisions — the estimates (4) and (5) do not require this. In fact, the factor $\mathrm{E}(y)/\mathrm{Var}(y)$ in (5) can be interpreted as a measure for the under- or over-dispersion of divisions per lineage with respect to the Poisson model where $\mathrm{E}(y) = \mathrm{Var}(y)$. In other words, if the Poisson model is assumed (then (40) describes the Compound Poisson distribution (CPD)) the mutation rate can be estimated directly from the data m, whereas if the mutation rate is known the accuracy of the Poisson model can be assessed. Finally, note that in the true system there are nonzero correlations between lineages – the early u_{ji} are shared amongst many cells – meaning that for a single population the m_j are not truly drawn from (40). While this does not affect the expected division rate (4), an inferred mutation rate will be influenced by a shared history, as it effectively reduces $\mathrm{Var}(y)$ and $\mathrm{Var}(u)$ (Fig. 3b).

1.7.2 Fluctuations of the mutational burden distribution

To investigate expected within- and between-patient variation of the mutational burden distribution we implemented individual-based stochastic simulations of single cell mutation acquisition. We start simulations with N cells and 0 mutations. Cells are picked randomly for division and acquire a number of mutations drawn from a Poisson distribution with rate parameter μ. In addition, cells may undergo symmetric or asymmetric divisions with a given probability p. If a cell divides asymmetrically, the novel mutations are added to that cell in the simulation. If a cell divides symmetrically, one cell in the population replaces another and novel mutations are added to the replaced and the dividing cell.

These simulation allow us to track the mutational burden distribution and its variance for arbitrary p, μ and large N over time. Realisations of these dynamics for $\mu = 1.3$ per cell division are shown in Fig. 7 and are compared to the experimental observation of the mutational burden distribution in [18]. We observe significant stochastic variations, especially pronounced for small stem cell population sizes N and low asymmetric division probabilities p. However, the true biological parameters are more likely to be a combination of large N and large p and therefore a mutation rate of $\mu = 1.3$ per cell division is unlikely to explain the observations in [18].

In Fig. 7 and Fig. 8 we show the likelihood that the ratio of Variance/Mean is within the experimentally observed interval $3 < \theta < 5$. Again we can see that for $\mu = 1.3$ the ability to explain the experimental observations is limited for any combination of parameters. Increasing the mutation rate to $\mu = 3$ in contrast can explain the experimental observations for a wide range of parameter combinations.

1.8 Data fitting pipeline

To estimate values of the model parameters from the data, we combine both prediction for the single-cell mutational burden as well as the mutation allele frequency distribution. The unknown parameters are those listed in Table 1, whereby the growth rate is implicitly defined from the mature population size and the maturation time as $\gamma = \log(N_M)/t_M$.

1.8.1 Estimating division rates from the single-cell mutational burden distribution

While the single-cell mutational burden distribution allows for direct estimation of the average number of divisions that occurred per lineage through Eq. (4), this does not directly provide the division rates, as these combine in the integrand on the lhs. To perform the integration we must first determine the expected contributions of each type of division (growth, symmetric, or asymmetric) to the mutational burden of a single lineage, as they — perhaps counter-intuitively — do not influence the expected burden equally.

Consider the system of N cells which obey the dynamics described in Section 1.1. At any point in time each cell describes a single lineage, and we are interested in the expected number of mutations added per lineage over time. Since divisions occur as independent Poisson events, we may treat the distinct types individually and simply add their contributions together to obtain the total burden increase over time. When an asymmetric division occurs the situation is simple: The single stem-type daughter cell acquires on average μ new mutations, which increase the average burden per cell by μ/N. Since these dynamics are Markovian, and events occur at rate $N\phi$ in the population, we obtain the average number of mutations acquired per lineage in a time Δt as

$$\Delta m_\phi = N\gamma \times (\mu/N) \times \Delta t = \phi\mu\,\Delta t \tag{43}$$

When a symmetric division occurs (as performed in the Moran process described previously) the situation becomes slightly more complicated. Following a single division we discern two disjunct outcomes: either two different cells are selected for replication and removal, or the same cell is selected for both. The former case occurs with probability $1 - 1/N$ and results in the average burden per lineage increasing by $2\mu/N$ (two daughter cells obtained on average μ new mutations), while the latter occurs with probability $1/N$ and causes the average burden to increase by μ/N (one of the daughter cells was removed).With these events occurring at rate $N\rho$ the expected increase per lineage after a time Δt is:

$$\Delta m_\rho = N\rho\mu\left[\left(1 - \frac{1}{N}\right)\frac{2}{N} + \frac{1}{N}\frac{1}{N}\right]\Delta t = \rho\mu(2 - 1/N)\Delta t \approx 2\rho\mu\,\Delta t \tag{44}$$

with the final approximation obtained in the limit of large N. For the pure growth divisions occurring at rate $N\gamma$ we take a similar approach, though we now consider an infinitesimal time increment dt to account for the varying population size. After a single division the average burden increase is $2/(N(t)+1)$, so that

$$dm_\gamma = N(t)\gamma\mu\frac{2}{N(t)+1}dt = 2\gamma\mu\frac{N(t)}{N(t)+1}dt \approx 2\gamma\mu\,dt \tag{45}$$

Thus, we find that the growth and Moran divisions on average add twice as many mutations to a lineage as the asymmetric divisions. Note that we obtain the average increase in lineage (the number of divisions in a cell's past) by setting $\mu = 1$ in the equations above. Plugging these results into the integral of (4), we find for the expected number of divisions per lineage at time t

$$y(t) = \int_0^t \left[2\rho\left(1 - \frac{1}{2N(\tau)}\right) + \phi + 2\gamma\left(1 - \frac{1}{N(\tau)+1}\right)\right]d\tau \tag{46}$$

Taking into account the different phases of evolution we can separate the integral into three parts

$$
\begin{aligned}
y(t) = &\int_0^{\log N_H/\gamma} 2\gamma\left(1 - \frac{1}{N(\tau)+1}\right) d\tau \\
&+ \int_{\log N_H/\gamma}^{t_M} \left[2\rho\left(1 - \frac{1}{2N(\tau)}\right) + \phi + 2\gamma\left(1 - \frac{1}{N(\tau)+1}\right)\right] d\tau \\
&+ \int_{t_m}^{t} \left[2\rho\left(1 - \frac{1}{2N(\tau)}\right) + \phi\right] d\tau
\end{aligned}
\tag{47}
$$

Denoting $\lambda = \rho + \phi$ the total rate of homeostasis divisions within the stem cell compartment, performing the integration we solve this for

$$
\lambda = \frac{R - 2\log\left(N_M + 1\right) + \log(4)}{-(1-p)(t - t_M)/N_M + (2-p)\left(t - t_M \frac{\log(N_H)}{\log(N_M)}\right) - (1-p)\, t_M \left(\frac{1}{N_H} - \frac{1}{N_M}\right) / \log(N_M)}
\tag{48}
$$

with $R = \mathrm{E}(m)/\mu$ the average number of divisions per lineage estimated from the mutational burden distribution. With μ estimated from [5], the remaining unknown parameters are t_M, N_H, N_M, and p. Finding the standard error on $\mathrm{E}(m)$ as $\sigma_{\mathrm{E}(m)} = \sigma_m/\sqrt{S}$ (with S the sample size) and sweeping the unknown parameters within reasonable limits ($t_M \in [0, 10]$, $N_H \in [0, 1000]$, $N_M \in [20'000, 500'000]$) gives an error interval for the expected λ.

1.8.2 Fitting to the lowest frequency of the VAF distribution

We must be cautious about attempting to directly fit realizations of Eq. (1) to an observed distribution in its entirety. Without knowledge of the variance across individual realizations for each possible allele frequency, there is no rigorous way to weight the errors from different frequencies to obtain a single best fit. Indeed, simulations suggest that the variance on the number of mutations per VAF grows with the frequency (Fig. 9), implying that a non-weighted fit would overemphasize fluctuations at one end of the spectrum. We therefore selected only the lowest frequency available in the sample – which is anticipated to be the best described by the expected value (Fig. 9b) – as the reference for parameter fitting.

For select values of t_M and N_H, we calculated the VAF distribution — by numerically solving Eq. (1) and applying the sampling operator Eq. (6) — at lattice points in the parameter space of $N_M \in \left[5 \cdot 10^3, 5 \cdot 10^5\right] \times p \in [0, 1]$. For each point (N_{Mi}, p_i) we compared the lowest frequency of the theoretical expected distribution $v_{1/S}$ with the value measured in the data, resulting in a 2D lattice of errors. From this lattice a continuous error function was obtained through spline interpolation, wherein we identified a zero-error line, which is the line of optimal fit shown in Fig 4c.

References

[1] Samra Turajlic et al. "Resolving genetic heterogeneity in cancer". In: *Nature Reviews Genetics* 20.7 (2019), pp. 404–416.

[2] James RM Black and Nicholas McGranahan. "Genetic and non-genetic clonal diversity in cancer evolution". In: *Nature Reviews Cancer* 21.6 (2021), pp. 379–392.

[3] Caroline J Watson et al. "The evolutionary dynamics and fitness landscape of clonal hematopoiesis". In: *Science* 367.6485 (2020), pp. 1449–1454.

[4] Steffen Rulands et al. "Universality of clone dynamics during tissue development". In: *Nature physics* 14.5 (2018), pp. 469–474.

[5] Benjamin Werner et al. "Measuring single cell divisions in human tissues from multi-region sequencing data". In: *Nature communications* 11.1 (2020), pp. 1–9.

[6] Einar Bjarki Gunnarsson, Kevin Leder, and Jasmine Foo. "Exact site frequency spectra of neutrally evolving tumors: A transition between power laws reveals a signature of cell viability". In: *Theoretical Population Biology* 142 (2021), pp. 67–90.

[7] Inigo Martincorena. "Somatic mutation and clonal expansions in human tissues". In: *Genome Medicine* 11.1 (2019), pp. 1–3.

[8] Mel Greaves and Carlo C Maley. "Clonal evolution in cancer". In: *Nature* 481.7381 (2012), pp. 306–313.

[9] Alex Cagan et al. "Somatic mutation rates scale with lifespan across mammals". In: *Nature* 604.7906 (2022), pp. 517–524.

[10] Iñigo Martincorena et al. "Somatic mutant clones colonize the human esophagus with age". In: *Science* 362.6417 (2018), pp. 911–917.

[11] Emily Mitchell et al. "Clonal dynamics of haematopoiesis across the human lifespan". In: *Nature* (2022), pp. 1–8.

[12] Federico Abascal et al. "Somatic mutation landscapes at single-molecule resolution". In: *Nature* 593.7859 (2021), pp. 405–410.

[13] Gladys YP Poon et al. "Synonymous mutations reveal genome-wide levels of positive selection in healthy tissues". In: *Nature Genetics* 53.11 (2021), pp. 1597–1605.

[14] Iñigo Martincorena et al. "Universal patterns of selection in cancer and somatic tissues". In: *Cell* 171.5 (2017), pp. 1029–1041.

[15] Lemonia Chatzeli and Benjamin D Simons. "Tracing the dynamics of stem cell fate". In: *Cold Spring Harbor perspectives in biology* 12.6 (2020), a036202.

[16] Marc J Williams et al. "Measuring the distribution of fitness effects in somatic evolution by combining clonal dynamics with dN/dS ratios". In: *Elife* 9 (2020).

[17] Rick Durrett. "Population genetics of neutral mutations in exponentially growing cancer cell populations". In: *The annals of applied probability: an official journal of the Institute of Mathematical Statistics* 23.1 (2013), p. 230.

[18] Henry Lee-Six et al. "Population dynamics of normal human blood inferred from somatic mutations". In: *Nature* 561.7724 (2018), pp. 473–478.

[19] Calum Gabbutt et al. "Fluctuating methylation clocks for cell lineage tracing at high temporal resolution in human tissues". In: *Nature biotechnology* 40.5 (2022), pp. 720–730.

[20] David Dingli and Jorge M Pacheco. "Allometric scaling of the active hematopoietic stem cell pool across mammals". In: *PLoS One* 1.1 (2006), e2.

[21] Chris Bailey et al. "Tracking cancer evolution through the disease course". In: *Cancer discovery* 11.4 (2021), pp. 916–932.

[22] Giulio Caravagna et al. "Subclonal reconstruction of tumors by using machine learning and population genetics". In: *Nature Genetics* 52.9 (2020), pp. 898–907.

[23] Sohrab Salehi et al. "Clonal fitness inferred from time-series modelling of single-cell cancer genomes". In: *Nature* 595.7868 (2021), pp. 585–590.

[24] Bora Lim, Yiyun Lin, and Nicholas Navin. "Advancing cancer research and medicine with single-cell genomics". In: *Cancer cell* 37.4 (2020), pp. 456–470.

[25] Michael Spencer Chapman et al. "Lineage tracing of human development through somatic mutations". In: *Nature* 595.7865 (2021), pp. 85–90.

[26] Richard Durrett. *Branching Process Models of Cancer*. 2015. DOI: 10.1007/978-3-319-16065-8_1.

[27] Marc J Williams et al. "Identification of neutral tumor evolution across cancer types". In: *Nature genetics* 48.3 (2016), pp. 238–244.

[28] Nicholas Williams et al. "Life histories of myeloproliferative neoplasms inferred from phylogenies". In: *Nature* 602.7895 (2022), pp. 162–168.

[29] Benjamin Werner et al. "Reconstructing the in vivo dynamics of hematopoietic stem cells from telomere length distributions". In: *Elife* 4 (2015), e08687.

[30] Cristian Tomasetti et al. "Cell division rates decrease with age, providing a potential explanation for the age-dependent deceleration in cancer incidence". In: *Proceedings of the National Academy of Sciences* 116.41 (2019), pp. 20482–20488.

[31] Iñigo Martincorena et al. "High burden and pervasive positive selection of somatic mutations in normal human skin". In: *Science* 348.6237 (2015), pp. 880–886.

[32] Benjamin Werner et al. "The cancer stem cell fraction in hierarchically organized tumors can be estimated using mathematical modeling and patient-specific treatment trajectories". In: *Cancer research* 76.7 (2016), pp. 1705–1713.

[33] Benjamin Werner. "Shining light on dark selection in healthy human tissues". In: *Nature Genetics* 53.11 (2021), pp. 1525–1526.

[34] Andrejs Ivanovs et al. "Human haematopoietic stem cell development: from the embryo to the dish". In: *Development* 144.13 (2017), pp. 2323–2337.

[35] Warren J. Ewens. "Discrete Stochastic Models". In: *Mathematical Population Genetics: I. Theoretical Introduction*. New York, NY: Springer New York, 2004, pp. 92–135. ISBN: 978-0-387-21822-9. DOI: 10.1007/978-0-387-21822-9_3. URL: https://doi.org/10.1007/978-0-387-21822-9_3.

[36] Daniel T Gillespie. "Exact stochastic simulation of coupled chemical reactions". In: *The journal of physical chemistry* 81.25 (1977), pp. 2340–2361.

[37] Warren J. Ewens. "Diffusion Theory". In: *Mathematical Population Genetics: I. Theoretical Introduction*. New York, NY: Springer New York, 2004, pp. 136–155. ISBN: 978-0-387-21822-9. DOI: 10.1007/978-0-387-21822-9_4. URL: https://doi.org/10.1007/978-0-387-21822-9_4.

[38] Motoo Kimura. "Solution of a process of random genetic drift with a continuous model". In: *Proceedings of the National Academy of Sciences* 41.3 (1955), pp. 144–150.

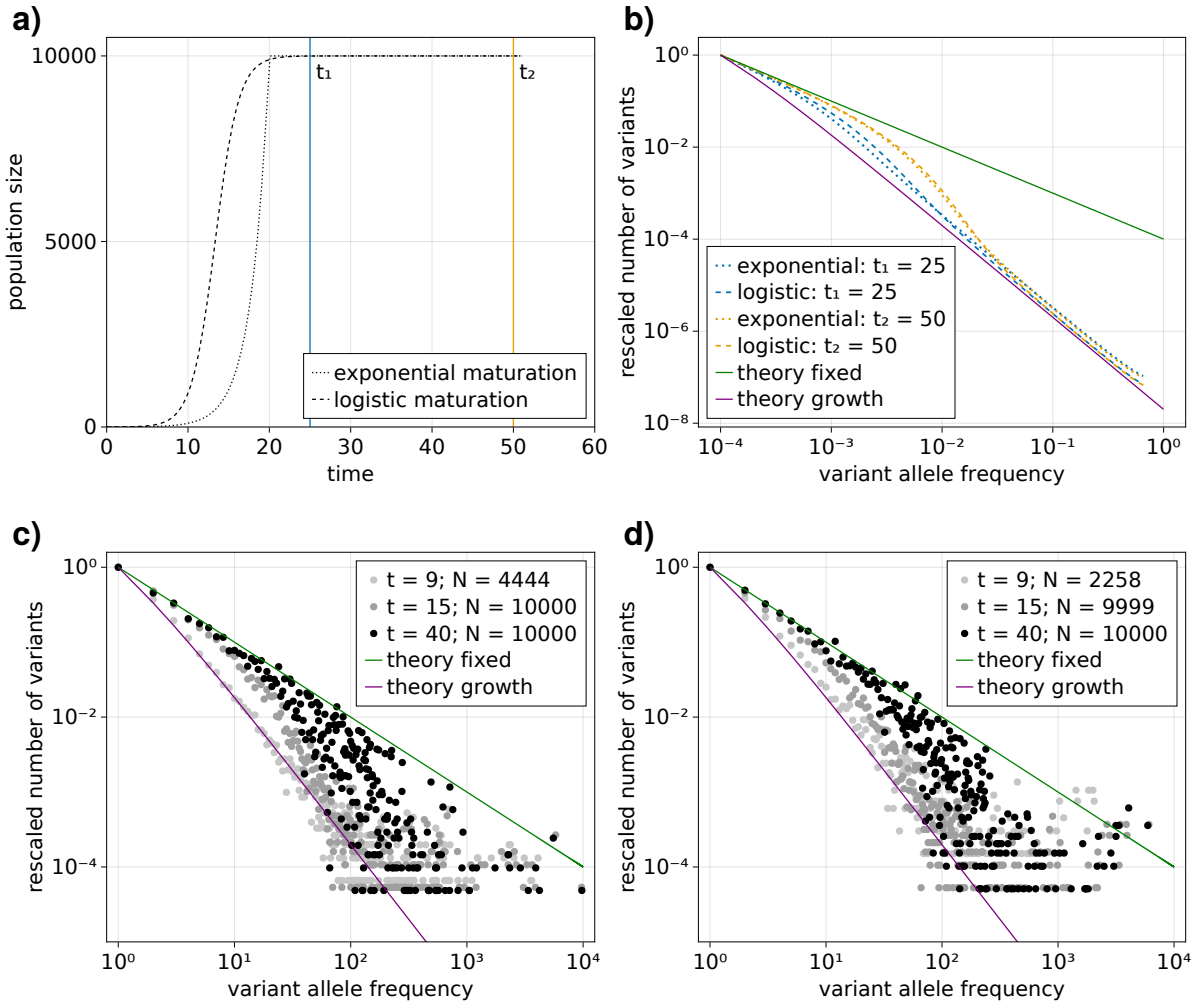

Figure 5. Comparison of an exponential and logistic growth model. (a) Population size over time for exponential (dotted) and logistic (dashed) growth functions. At the point of maturity ($t = 20$) the exponential function reaches the population capacity ($N_M = 10'000$), and the logistic function equals $0.99N_M$. The time points at which the VAF spectra are measured are indicated by solid vertical lines: $t_1 = 25$ (blue) and $t_2 = 50$ (orange). **(b)** Comparison of the expected VAF spectra, calculated with Eq. (1), in the exponential (dotted) and logistic (dashed) growth models measured at the time points t_1 and t_2. For reference, the theoretical predictions for an exponentially growing population without cell death and a constant population in the long time limit are shown as solid purple and green lines respectively.

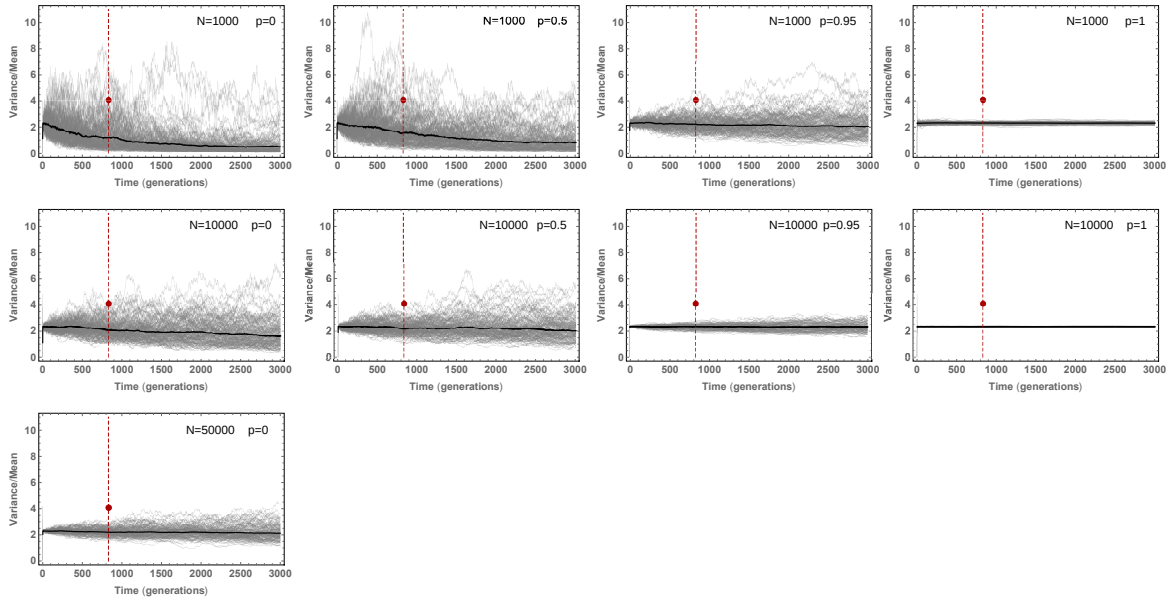

Figure 6. Stochastic simulations of the Variance/Mean of the mutational burden distribution over time for a per cell division mutation rate of $\mu = 1.3$ and varying stem cell population size N and asymmetric division probability p.Stochastic fluctuations are pronounced for small population size N and low asymmetric division probability p.

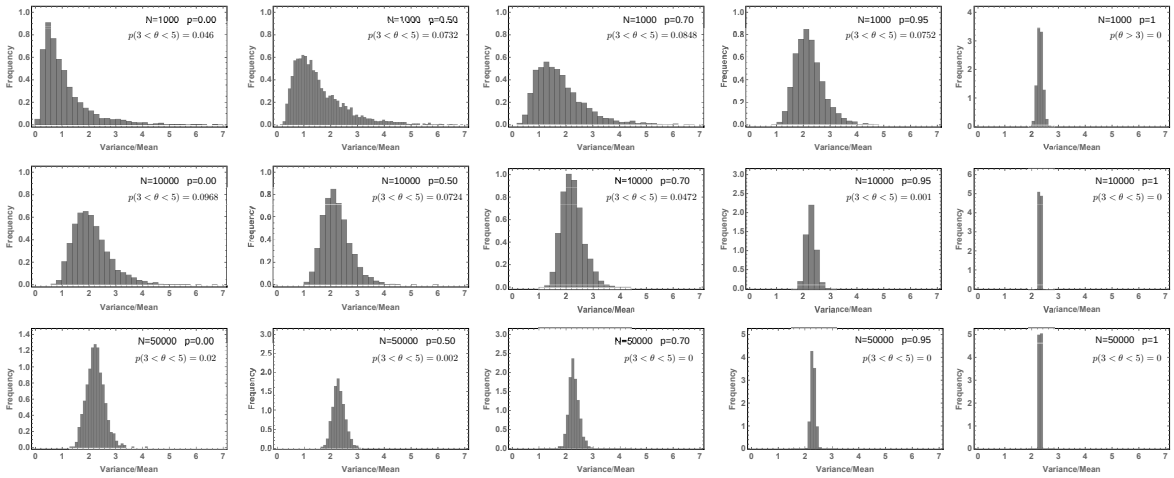

Figure 7. Likelihood of the Variance/Mean to be in the interval $3 < \theta < 5$ for a per division mutation rate of $\mu = 1.3$.

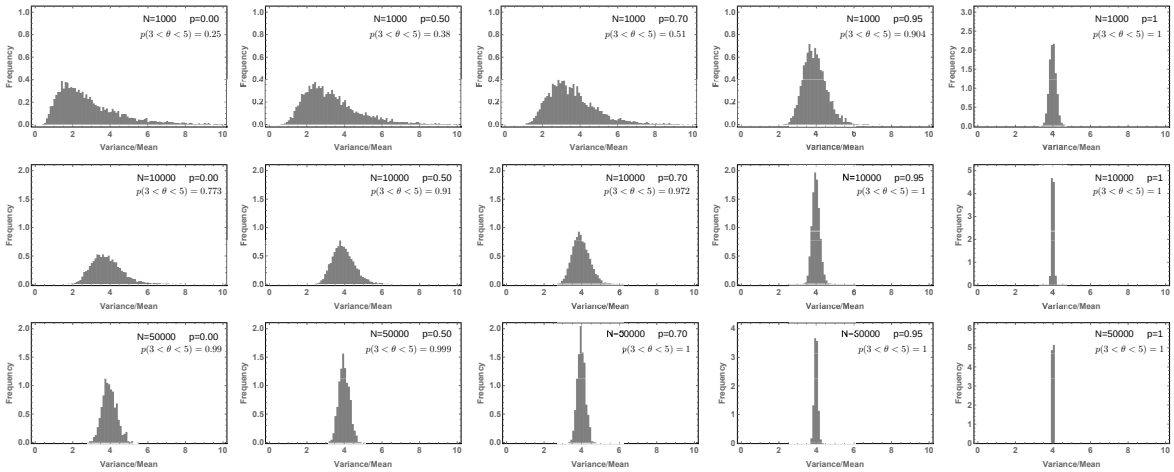

Figure 8. Likelihood of the Variance/Mean to be in the interval $3 < \theta < 5$ for a per division mutation rate of $\mu = 3$.

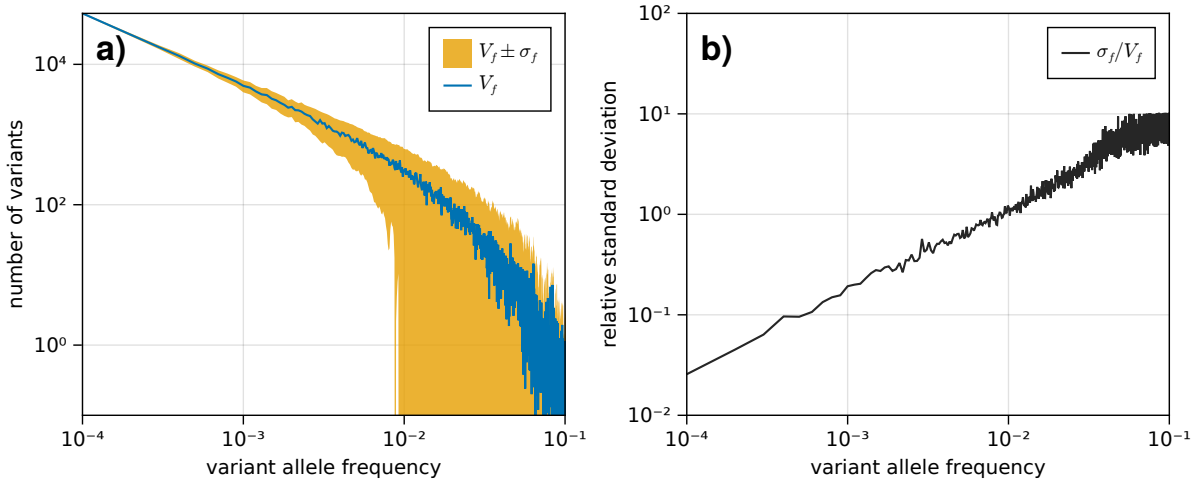

Figure 9. The standard deviation on the VAF spectrum increases for higher frequencies. a) The VAF spectrum V_f averaged across 100 simulations of a population evolved according to the model described in section 1.1. The standard deviation from the mean is shown as the band $V_f \pm \sigma_f$ around the average. **b)** The standard deviation across all simulations for each frequency $f = 1/N, 2/N, \ldots$, scaled by the average spectrum V_f.